Silicon pore optics for high-energy optical systems

Girou, D.A.

2

SILICON PORE OPTICS REALIZATION

Silicon Pore Optics (SPO) uses commercially available monocrystalline double-sided superpolished silicon wafers as a basis to produce mirrors that form low-mass high-resolution X-ray optics. The technology has been invented by cosine measurement systems and the European Space Agency (ESA) and developed together with scientific and industrial partners to mass production levels. It leverages techniques and processes developed over decades by the semiconductor industry to handle, process, and clean silicon wafers and plates. SPO is an enabling technology for large space-borne X-ray telescopes such as Athena, operating in the 0.2 to 12 keV band, with angular resolution aiming for 5 arc seconds.

Parts of this chapter are based on an invited chapter for the Handbook of X-ray and Gamma-ray Astrophysics (Eds. C. Bambi and A. Santangelo, Springer Singapore, expected in 2022). Contributors to this invited chapter are Nicolas M. Barrière[1], Marcos Bavdaz[2], Maximilien J. Collon[1], Ivo Ferreira[2], David Girou[1], Boris Landgraf[1], and Giuseppe Vacanti[1].

[1] cosine measurement systems, Warmonderweg 14, 2171 AH Sassenheim, The Netherlands.
[2] European Space Agency, ESTEC, Keplerlaan 1, 2200 AG Noordwijk, The Netherlands.

2.1 Introduction

Silicon pore optics (SPO) are a new type of X-ray optics designed to enable future space-borne X-ray observatories such as Athena [1]. They are being developed by the European Space Agency (ESA), in collaboration with academic and industrial partners [2, 3]. These high-performance, modular, lightweight, yet stiff, high-resolution X-ray optics allow missions to reach an unprecedented large effective area of a few square meters, operating in the 0.2 to 12 keV band and with an angular resolution aiming at being better than 5 arc seconds. To this end, custom-made assembly tools and processes have been developed to build SPO using direct silicon bonding[4, 5]. SPO plates are single-sided ribbed rectangular silicon substrates assembled into high-performance optics by direct bonding them on top of each other. In this chapter, we present how silicon pore optics plates are produced, coated, activated, and stacked into high-performance, self standing X-ray optics. Then, we further investigate how these stacks are assembled into mirror modules and characterized.

2.2 Production of SPO mirror plates

With the technology spin-in from the semiconductor industry, mass production is being set up and standardized processes are being developed in order to manufacture SPO mirror plates in high quality, large quantity, and at relatively low cost. The production of SPO mirror plates starts with carving out ribs into 300 mm wafers. This process is effectively performed by removing material from the wafer down to the desired membrane thickness. Subsequently, rectangular plated are diced off the wafer, with the ribs along the direction of travel of the X-rays. The orientation of plate ribs and edges is aligned with the crystal planes of the silicon to ensure correct bending. The top side of the mirror plate is the reflective side (Figure 2.1, a)), and at the bottom is the ribbed side (Figure 2.1 b)) with the ribs parallel to each other. The plates currently manufactured have rib pitch varying from 1.0 mm to 2.4 mm with rib width of 0.17 mm.

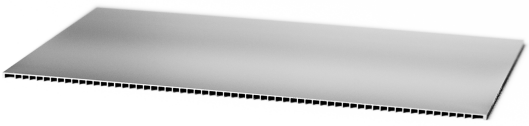

(a)

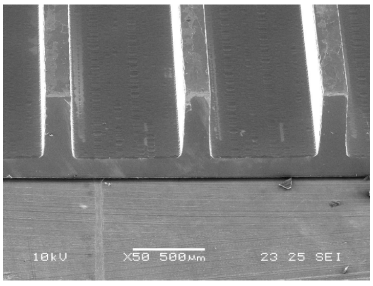

(b)

Figure 2.1: (a) Example of a SPO mirror plate with its reflective side on top, and ribbed side facing down. (b) Scanning electron microscope image of the ribs of a SPO mirror plate.

The SPO mirror plates feature a thickness gradient along the rib direction to ensure that all the plates within a stack are confocal. The plane of the ribs is at an angle with the reflective side, referred to as the wedge angle. The challenge is to implement this angle with a linear profile, and without increasing the roughness of the surfaces. Two approaches have been developed to realize the wedge angle. A thickness gradient is either created by wet-chemical etching, or by IBF. A wedge accuracy better than 1% has been obtained with the wet-chemical processing, while the IBF is still under development. The advantage of IBF is that the TTV of wafers can be improved and reduced to potentially less than 10 nm in the same production step as the wedge processing.

Cleanliness is a crucial parameter for the production stacks. Particles on the plate surface can reduce bonding area and distort the optical figure. For this reason, SPO mirror plate production is performed in high-quality clean room environments of ISO 6 and ISO 5, and with specific equipment for also reducing the risk of organic contamination which can have a negative impact on the bondability of SPO mirror plates.

2.3 Development of coatings

The reflectivity of SPO mirror plates can be enhanced by deposition of thin-film coatings. The effectiveness of the coating is thereby described by the effective area of the optics. It depends on the collecting area and the efficiency of the mirrors in reflecting high-energy photons. The broadest energy window can be achieved with combinations of high-Z (e.g. Au, W, Mo, Pt and Ir) and low-Z materials (e.g. Si, SiC, C, DLC and B4C). Figure 2.2 shows an example of the computed on-axis effective areas for different reflective coatings for the Athena telescope energy range. The effective area is significantly larger with the addition of high-Z/low-Z bilayer coatings compared to the effective area of uncoated SPO mirror plates. In addition, multilayer coatings consisting of superimposed bilayers of high-Z/low-Z material can be applied to further increase the X-ray response of the optics at higher energies [6].

The SPO mirror plates feature a patterned coating on their reflective side in order to enable direct silicon bonding [4, 5] (see Section 2.5). The patterning of the coating is performed via optical lithography. This process, sketched in Figure 2.3, consists of the following steps. Firstly, a photosensitive polymer is deposited on the reflective side of the SPO mirror plate. In a second step, a patterned photoresist layer is created by exposing the photosensitive polymer to ultraviolet light and developing it by immersing the sample in a chemical solution. Subsequently, an X-ray reflective coating is deposited using a sputtering deposition technique. Finally, chemical lift-off is performed to remove the coated photoresist resulting in a patterned coated SPO mirror plate.

Direct current magnetron sputter deposition (MSD) has been applied for producing X-ray reflective coatings on mirrors of a number of X-ray telescopes, and as such, is a method with a good track record. It is a low-cost and well-controlled process. Particularly, iridium films with a thickness of 30 nm have been sputtered onto the Chandra telescope mirrors [8], and Pt/C and W/Si bilayer systems have been used for the NuSTAR

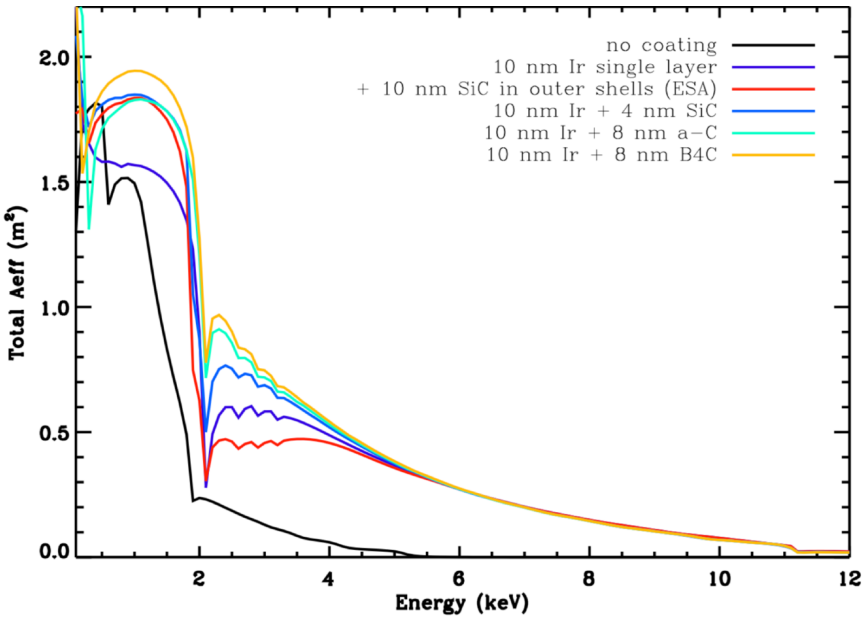

Figure 2.2: On-axis total effective areas for different reflective coatings for the Athena telescope energy range. Note that a significant increase in effective area can be expected at 1 keV if e.g. a B_4C overcoat is used. Credit: DTU [7].

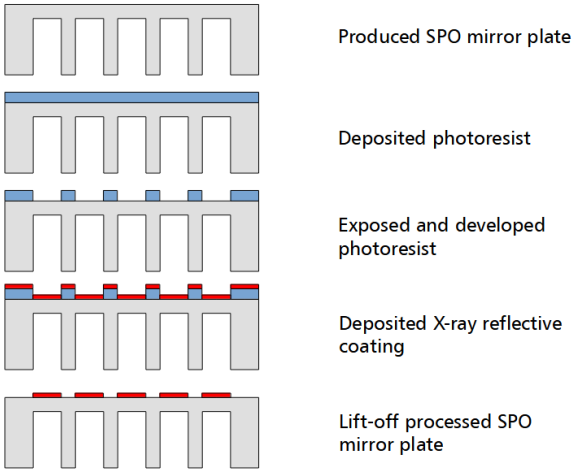

Figure 2.3: Schematic of optical lithography for SPO mirror plate with patterned X-ray reflective coating.

telescope mirrors successfully [9].

The SPO mirror plate coating process takes place at cosine using an industrial, high-throughput magnetron sputtering system [10] (Figure 2.4). It features three magnetrons for coating target materials and a plasma cleaning system in order to clean substrates from organic materials before a coating deposition run [11]. With this system, substrates as large as full 300 mm wafers can be coated with various high-Z materials such as tungsten, molybdenum, platinum and iridium and low-Z materials such as silicon, silicon carbide, carbon, diamond-like carbon, and boron carbide.

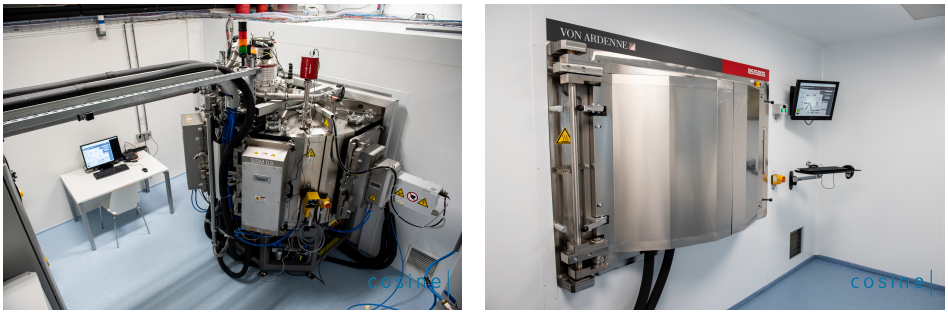

(a) (b)

Figure 2.4: Coating machine at cosine: (a) back side and (b) clean room side of the system.

The left photograph in Figure 2.5 shows an example of the reflective side of a produced patterned iridium-coated SPO mirror plate. In the right photograph, the coating stripes can clearly be distinguished from the silicon bonding areas.

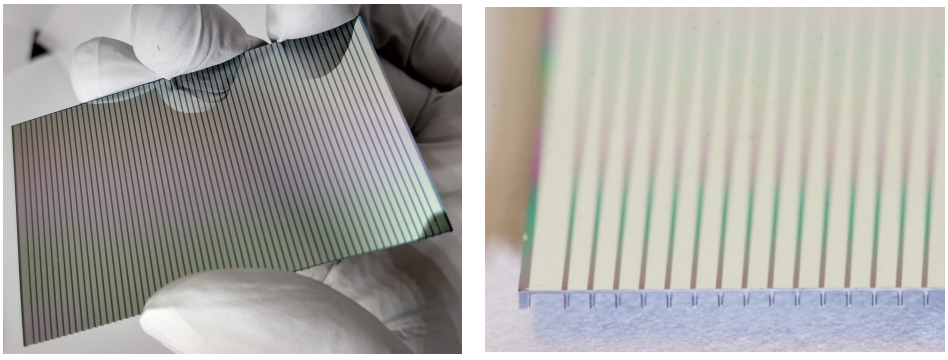

(a) (b)

Figure 2.5: (a) SPO mirror plate with patterned coating of 10 nm iridium. (b) close-up view of a SPO plate with patterned iridium coating. The uncoated tracks are clearly visible above the ribs.

(a) (b)

Figure 2.6: Plate cleaning container (a) and fully automated wet bench (b) for chemical cleaning and activation of SPO mirror plates at cosine.

2.4 Cleaning and activation

Cleanliness is paramount to the SPO technology. The mirror plates are cleaned in industrial wet-benches with a SC-1 cleaning [12] and then dried.This results in hydrophilic ('activated') surfaces, free of particulate contamination or drying stains. The hydrophilic surfaces are key to direct silicon bonding, as explained in the next section.

The photographs in Figure 2.6 show the fully automated cleaning wet bench at cosine, which is used to prepare the SPO mirror plates for stacking.

2.5 Stacking of mirror plates

SPO stacks hold together and maintain their shape without adhesive between the mirror plates. This direct bonding process can take place at room temperature and is widely used to join glass or silicon surfaces to each other [4, 5]. The two mating surfaces need to be chemically prepared (i.e. activated) and need to be clean, smooth, and conforming for a direct bond to take place. After activation, a thin layer of OH- groups is present on both the ribbed and the reflective sides of each mirror, forming silanol (Si-OH) groups [13]. These absorbed water molecules form a bridge (Si-OH+HO-Si) across the two bonding surfaces that is maintained via Van-der-Waals forces for temperatures ranging from 10°C to 110°C [13]. Furthermore, post-stacking thermal treatment, such as annealing above 110°C, enables the silanol bonds to transform into stronger siloxane (Si-O-Si) bonds [13]. During annealing, the interface is drying steadily and siloxane bridges form across the bonding surfaces, but for temperatures below 1000°C, the bonding energy is limited by the area in contact, which is itself limited by surface roughness [13]. Annealing at temperatures above 1000°C can increase the contact area through viscous flow of the oxide, which then fills up the micro-gaps at the interface to form additional siloxane bonds [13]. However, environmental testing (see Section 2.8) indicates that the bond energy is large

enough to survive shock and vibration testing, meaning that annealing stacks at temperatures between 150°C and 1000°C is sufficient. Note that the excess water can also exude over time and siloxane linkage can form after months of storage [13].

The plates are stacked on a concave mandrel, starting with a plate placed with reflective side in contact with the mandrel and ribs pointing inwards, called base plate. The mandrel is polished with the design shape of the stack, can be cylindrical or conical, and can feature additional meridional curvature. The next plate is then brought into a similar shape as the base plate by using a die, a tool with the same figure as the mandrel. The plate is attached with the mirror surface to the die, resulting in the ribs pointing outwards. The two plates are brought into close contact such that the two sets of ribs make contact and that direct bonding starts. At this moment, the plate copies the shape of the mandrel and becomes the first reflective plate of the stack. The die then releases the plate and the process can be repeated, with the only difference that the next plates are bonded with their ribs to the mirror surface of the upper plate in the stack. At the end of the process, the stack is released from the mandrel and keeps the desired shape through the acting bond forces and the stiffening effect of the ribs. To achieve high angular resolution, it is important to replicate the initial figure of the mandrels with minimum systematic and stochastic errors. Cleanliness of the plates, mandrel and die is of prime importance to avoid degrading the figure with bumps created by trapped particles plate after plate. Systematic slope errors can be minimized with optimized plate design and stacking approach.

Note that when it is curved, the mandrel defines only the outer starting radius of a stack. With each plate added, the stacks' sagittal radius of curvature becomes smaller by the thickness of the mirror plate. In the case of double-reflection optical design, such as Wolter I, it is important to align the ribs to several microns. This minimizes the loss of open area as the two stacks are aligned behind each other.

2.6 Stacking robots

Automated stacking robots have been developed to meet the mass production and quality requirements of SPO technology: automation provides cost-efficiency, improves repeatability for large series, and ensures the highest standard of cleanliness. The robots are composed of a robotic arm equipped with a plate gripper, a die attached upside down, and a mandrel resting onto an hexapod (Figure 2.7). The hexapod is on a linear translation stage that allows moving the mandrel and the stack from the die to an optical metrology system.

The stacking process starts with a batch of several tens of plates loaded in a container that are cleaned and activated (Figure 2.6). The container is loaded into the robot, which is placed inside an ISO-class 5 clean area to keep the plates from particulate contamination. The robot extracts the first plate from the container, aligns it to the gripper, and places it on the mandrel, as described in Section 2.5. A second plate is extracted, aligned to the gripper and attached to the die with the ribs pointing downwards. The mandrel

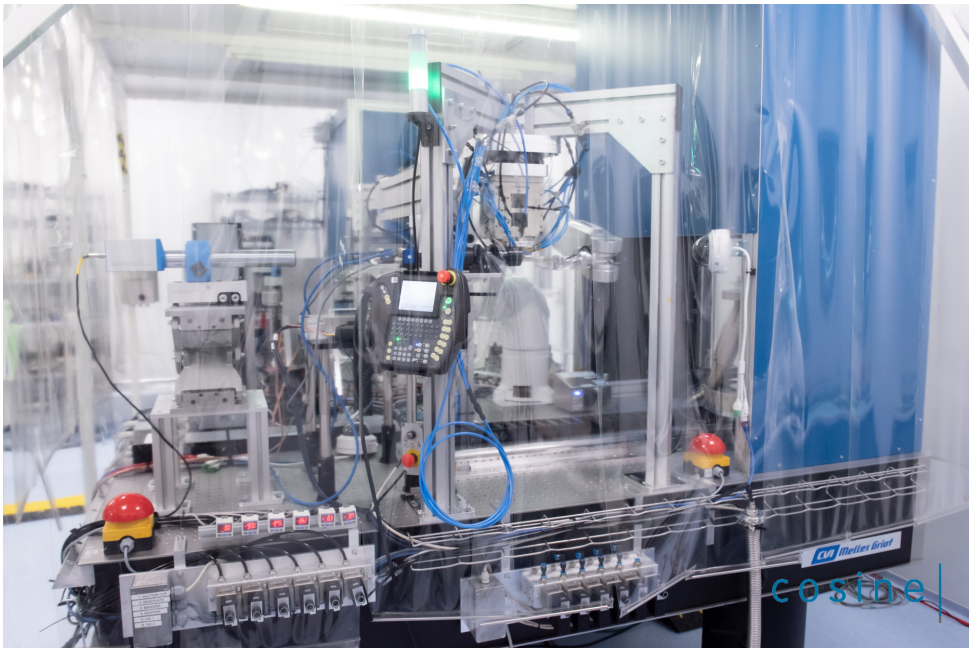

Figure 2.7: Stacking robot inside a cleanroom, as installed at cosine. It is equipped with a robotic arm to extract plates for stacking. A hexapod allows aligning the mandrel to the die. The blue box on the right is an optical metrology system that can measure the figure and cleanliness of each plate after having been stacked.

and die are brought into close contact until the ribs align and the bond is created. Then the die releases the plate. The first reflective plate is now bonded to the base-plate. The stack is translated to the in-situ metrology, which measures the figure of the bonded plate, determining not only the shape, but also the cleanliness and therefore the quality of the bond. The robot then proceeds to extract the next plate, attaching it to the die. The stacking process repeats, this time with the ribs bonding to the mirror surface of the stack on the mandrel.

The process repeats until the desired stack height is reached. Stacks between 10 and 70 plates have been manufactured, 35 plates being the most common so far. The stacking process takes about 5 minutes per plate and can run completely autonomously. Once the stack is finished, it is released from the mandrel and a final inspection is performed to measure the outer geometry and to visually check for defects.

Prior to stacking, the mandrel axis is aligned with the die axis. The plate gripper, which is the reference for the plates alignment, is also aligned with respect to the die and mandrel. A robot is configured for one specific set of stacks defined by its mandrels and plate types. The robot needs to be reconfigured to produce stacks of different radii, plate geometry or figure.

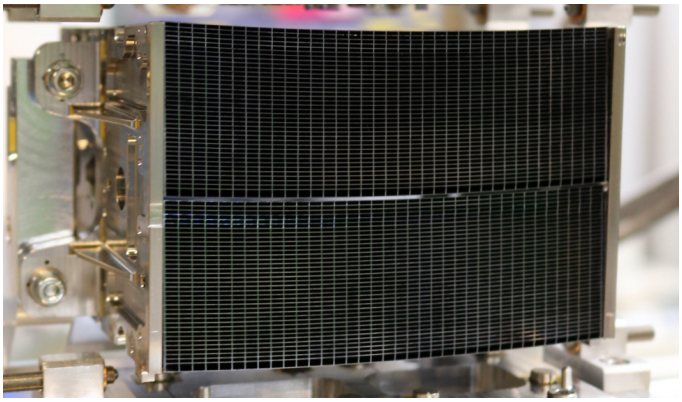

Figure 2.8: Row-08 MM seen from the exit side. The two secondary stacks are visible, each with 37 mirror plates in addition of their base plate. Bracket A, with its two ears, is visible in this view.

2.7 Mirror modules

SPO consists of stacks of mirror plates, which shape is driven by the mandrels used. In the case of a Wolter I optical design, two different stack shapes are needed: primary and secondary stacks for the two reflections. When aligned after each other, these stacks form a so-called X-ray optical unit (XOU). The fact that the primary and secondary stacks are initially disjoined represents a challenge as their relative alignment can influence greatly the optical quality of the XOU. It is required to co-align their optical axis and align the mirror plates ribs and membranes. Then this alignment must be frozen. This freezing is done by gluing two side plates, commonly referred to as brackets, to the stacks, forming a mirror module (MM). A MM is thus a self-standing X-ray focusing optics with mechanical interfaces. The development of MMs has been been driven by Athena so far. In the current design, Athena MMs are made of two XOUs co-aligned to be confocal, glued within one pair of brackets (Figure 2.8).

The brackets are made of an austenitic nickel-iron alloy containing 36% nickel (Invar 36), a material with very low coefficient of thermal expansion of 1.2×10^{-6} K^{-1}, close to that of silicon 2.6×10^{-6} K^{-1}. Their role is to freeze the alignment of the stacks, protect the stacks, provide interfaces between the MM, and any support structure or mount, and provide a mechanical reference for the optical axis of the MM. The brackets can also provide interfaces to baffles or aperture mask. Low-outgassing and low-shrinkage epoxy is used to fixate the brackets to the sides of the stacks. The interface points of the brackets are called *ears* (visible on the right hand side of Figure 2.8).

The alignment strategy is as follows [14, 15]: the brackets are aligned with respect to each other using a tool providing six degrees of freedom to each bracket. The primary stack is then glued within the brackets. This alignment relies on mechanical metrology with a coordinate measurement machine (CMM). This assembly is then brought

to a synchrotron facility where a monochromatic, low-divergence, X-ray pencil beam is available. Currently this is done at the X-ray Parallel Beam Facility 2 (XPBF 2) synchrotron beamline, which is installed in the laboratory of the Physikalisch-Technische Bundesanstalt (PTB) at the synchrotron radiation facility BESSY II in Berlin [16]. An additional beamline is planned to become operational in 2022 at the ALBA synchrotron facility in Barcelona [17]. XPBF 2, tailored for the development of Athena's MMs, provides a 1-keV beam monochromatized and collimated by a toroidal mirror with multi-layer coating, allowing beam dimensions between 0.05×0.05 mm^2 and 7×7 mm^2. The detector is placed at 12 m $\pm$ 0.5 m from the sample, and its position is monitored by a laser tracker.

At XPBF 2, the direction of the incident beam is used as optical axis for the MM. The primary stack, already glued within the brackets, is aligned to bring its optical axis parallel to the beam. Then the secondary stack is brought in and the rest of the alignment is done in double reflection. The secondary stack is aligned with respect to the first stack to minimize the intersection of the ribs and membrane (i.e. maximize throughput of the XOU), bring the PSF at the nominal position, and obtain the best possible optical quality (co-align the stacks' optical axes).

Pencil beam raster scans are used to determine the three-axis orientation of the primary stack with respect to the beam, as well as of the secondary stack with respect to the primary stack [14]. The position of incidence of the beam onto the primary stack as well as the position of the beamspot recorded on the camera are reconstructed in a common coordinates system. An analytical three-dimensional model of the optic is used in a ray-trace function that transforms incident position into position on the camera. This function is used to fit the orientation of a stack in single reflection or double reflection. This method allows precise and deterministic alignment.

2.8 Ruggedisation

As SPO development progresses, it is necessary to validate the technology under launch and orbit environmental conditions [18]. Payloads undergo high levels of vibrations and shocks during the rocket launch and fairing separations. It is therefore crucial to check that the MMs are robust enough to withstand such conditions and ensure that their mechanical stability and optical performance will remain stable before, during, and after launch. Environmental testing also allows identifying potential design issues and correcting them. This is the process of ruggedisation where a piece of equipment is made stronger and more resistant.

Thanks to its modular nature, SPO can be tested at MM level. MMs are submitted to vibration and shock tests, in accordance with Athena's launch vehicle and mission requirements. The MMs are characterized with X-ray before and after each test to verify that the optical performance remains unchanged (Section 2.9). MMs are first integrated into a device under test (DUT, see Figure 2.9) that is representative of a mirror structure and enables interfacing the MM with test equipment (shock table, shaker, vacuum

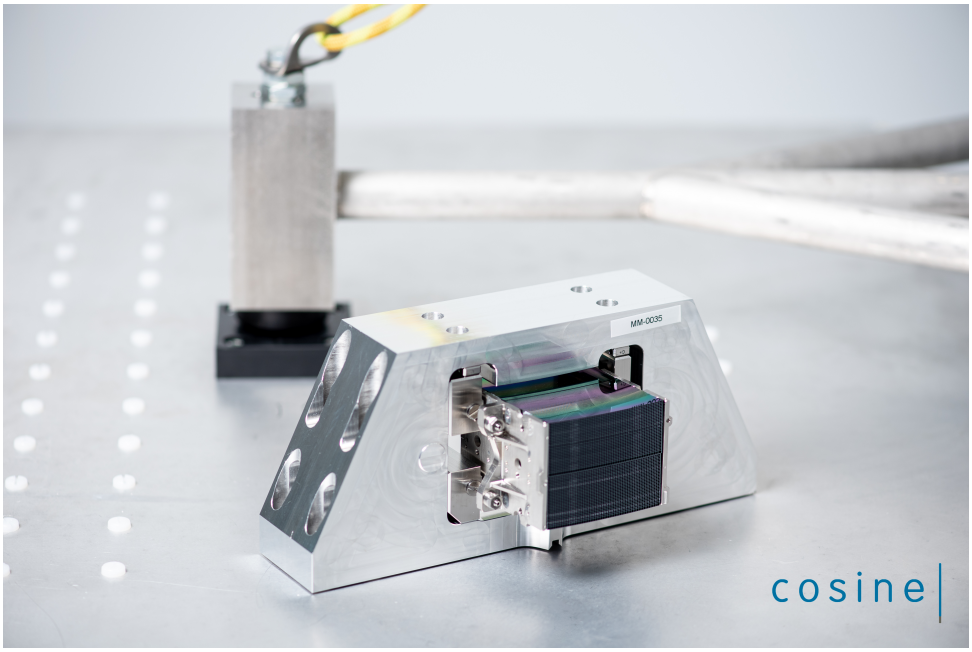

Figure 2.9: MM integrated into a device under test (DUT), laying on a shock table. The hammer can be seen resting on an anvil in the background.

chamber).

Vibration testing consists of two steps performed successively: sine qualification and random qualification tests. Two triaxial acceleration sensors (pilots) are mounted to the test mount to control the shaker input to the MM. The dynamic response of the MM is monitored on both brackets, close to the MM center of mass. Two single axis accelerometers are also used to monitor the dynamic transfer over the mechanical shims. These mechanical shims are used to preload the dowel pin (DP) flexures used to mount the MM, and to statically mimic the expected dynamic structural distortions of the mirror structure during low frequency (sine) and vibro-acoustic (random) mission phases. The Athena sine qualification test levels are shown in Table 2.1.

For the random test, Athena qualification and used notched levels are presented in Table 2.2. All random runs at qualification level are preceded by a low level ramp up, meaning a sequence of runs at -12 dB, -9 dB, -6 dB, and -3 dB for 30 seconds each. These runs are used to predict the 0 dB response levels at the MM center of mass and to check that the design limit load (DLL) values are not exceeded.

Frequency signature test runs (also called resonance searches) are performed before and after each high level qualification test run to detect any potential changes in structural behavior of the MM or test setup. A test run is considered successful if the change

Table 2.1: Athena sine qualification test levels for in-plane and out-of-plane directions.

Excitation direction	Frequency	Amplitude	Sweep rate
In-Plane (X, Y)	5 Hz 17 Hz 100 Hz	±11 mm 13 g 13 g	2 Oct/min
Out-of-plane (Z)	5 Hz 19 Hz 100 Hz	±11 mm 16 g 16 g	2 Oct/min

Table 2.2: Athena random qualification test levels with notching. Each test shall last 2 min per axis.

Direction	Frequency	Power Spectral Density (PSD)	Overall input
X	20-100 Hz 100 Hz 100-200 Hz 200-400 Hz 400-2000 Hz	+10 dB/Oct 0.05 g^2/Hz 0.20 g^2/Hz 0.05 g^2/Hz -15 dB/Oct	9.3 g-rms
Y	20-100 Hz 100 Hz 100-200 Hz 200-400 Hz 400-2000 Hz	+10 dB/Oct 0.05 g^2/Hz 0.20 g^2/Hz 0.05 g^2/Hz -15 dB/Oct	9.3 g-rms
Z	20-100 Hz 100 Hz 100-200 Hz 200-400 Hz 400-2000 Hz	+10 dB/Oct 0.05 g^2/Hz 0.70 g^2/Hz 0.05 g^2/Hz -15 dB/Oct	6.0 g-rms

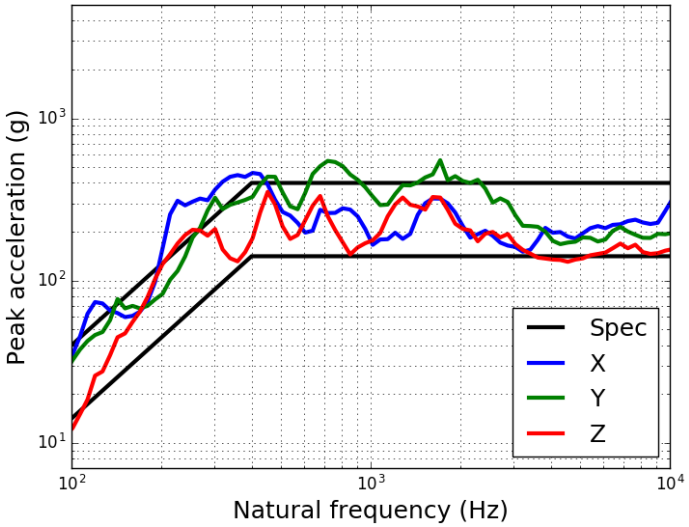

Figure 2.10: Shock Response Spectrum (SRS) of the shock applied to a MM. The qualification level with a margin of +6 dB and -3 dB define a specification (spec) band delimited by the black lines in the plot. Despite the peak acceleration being outside of the specification band for some frequencies, this SRS is considered excellent, and the test successful.

in frequency is less than 5%.

Shock testing is performed with a shock table and shock levels are defined by a shock response spectrum (SRS). Mechanical shims are used to preload the DP flexures similarly to the vibration test. There, the preloading and SRS level simulate mirror structure distortions during one of the most dramatic event of the launch sequence as seen by the payload: the fairing separation. Figure 2.10 displays a SRS as measured on the test mount (also called input SRS) of a MM. Note that the SRS is isotropic, enabling the testing of all three axis in a single shock. Two high-speed cameras, each looking at one side along the optical axis, are used to assist in identifying failures, as well as their modes. Resonance searches are also performed to check on the structural integrity of the MM.

SPO stacks have been tested as standalone items, then again once assembled into a MM for the different radii used for development (representative of the inner-most, middle, and outer-most radii of Athena). At the time of writing, the actual Athena flight configuration is also starting to be tested with the first row-08 MM having passed vibrations tests at qualification levels. Such testing campaigns at qualification levels will continue and extend to all rows of Athena, further ruggedizing SPO technology in general. For the flight model of Athena, each MM will undergo a workmanship test consisting of random vibration tests at acceptance level; additional environmental tests will be conducted at the mirror assembly level once the MM are integrated into the mirror structure.

2.9 X-ray characterization

Optical metrology of the SPO stacks taken during manufacturing produces a wealth of information on the eventual performance of the optics at X-rays. However, regular X-ray characterization remains an important part of the development process of the optics, as it is done at the same energy and incidence angle used during the actual use of the optics.

2.9.1 SPO stack characterization

Given the number of SPO stacks that are made, and the fact that individual stacks are not imaging systems, it has long been recognized that a dedicated facility with a high flux of X-rays is required to meaningfully support the development of the optics [19–22]. Characterization by means of a low-divergence (≈ 1 arcsec) pencil beam of X-rays, as opposed to the more customary full-flood illumination, makes it possible to probe the surface of each plate in a stack with high spatial resolution, and arrive at the characterization of the surface slope errors and of the millimeter-scale defects contributing to the widening of the beam. At the time of writing, two dedicated beamlines are available in the PTB laboratory at the BESSY II synchrotron [20, 22], and an additional beamline is being assembled at ALBA [17] (Section 2.7).

Samples are characterized by moving them in a rectangular pattern of columns and rows through a $100 \times 100\,\mu\text{m}^2$ X-ray beam. In Figure 2.11 we show how the samples are placed in the beam and measured. Scan columns are spaced usually by ≈ 2 mm, and scan rows are spaced by $100\,\mu$m. This so-called *standard scan pattern* probes only a fraction (about 5 %) of the total reflecting area in an SPO stack. Tests have shown that the results obtained in this manner are representative of the complete surface. That is, making the scan columns more densely spaced, or using overlapping beams, does not add new information on the properties of the stack derived from the data.

The data collected during a standard scan is processed to identify and isolate the reflected X-ray beam, then characterized by its centroid and RMS length and width. After this morphological characterization, the positions of the images and the sample in the laboratory frame are determined and converted to a common coordinate frame for further analysis. Each reflected beam probes between 5 and 10 mm along each of the pores, depending on the type of stack and the angle of incidence used in the measurement. Maps of the variation of the RMS length of the images already reveal good and bad areas on each plate.

A global quality indicator of the properties of the reflecting surface is derived by superimposing all the reflected images on their barycenters and calculating the half energy width (HEW) of the resulting image. This indicator is called the *on centroid performance* of the sample and is usually expressed in units of the HEW of the direct beam, and it represents the average surface quality on length scales of the order of a few to several millimeters.

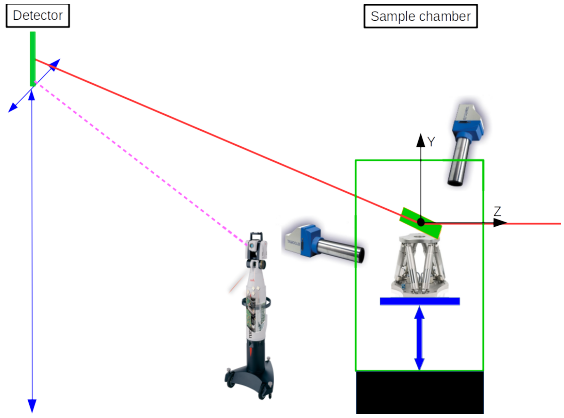

Figure 2.11: Logical view of a beamline dedicated to the assembly and characterization of SPO. The synchrotron X-ray beam travels from positive to negative Z (red). The sample is loaded inside a vaccum chamber (green) on a platform with six degrees of freedom and moved in front of the X-ray beam. During a measurement, the incidence angle of the X-ray is kept constant through the use of two autocollimators. The reflected beam is intercepted by a detector, whose position is monitored with a laser tracker.

More complex metrics can be obtained by processing the data further. A model of the stack is introduced, and the expected position of the barycenters of the reflected X-ray beam is calculated. By comparing the expected and the measured positions, a displacement vector is obtained for each reflected image. All the images are then superimposed on the common barycenter, where they would all end up if the SPO stack behaved ideally, and shifted by the displacement vector calculated. The HEW of the resulting image (Figure 2.13) is a metric of the optical quality of the stack, and it represents the contribution of the stack to the optical quality of a pair of stacks arranged to form an imaging system. This indicator is called the *on-model centroid performance* of the sample.

Data from the raster measurement can be used to derive a variety of performance indicators related to the optical quality of the stack. We mention here three of them, illustrated in Figure 2.12, they are:

- The broadening of the reflected beam, a marker of short length-scale errors;
- The (best-fit) meridional curvature, a marker of global figure errors;
- The difference between the measured and expected position of the reflected beam taking into account the best-fit meridional curvature, a marker of long length-scale figure errors.

The same analysis that leads to the calculation of the displacement vectors is also able to estimate the local surface normal seen by the X-ray beam, and the difference between ideal and actual surface normal. This information is coded in a *synoptic slope error map*, an example of which is shown in Figure 2.14. The map codes information

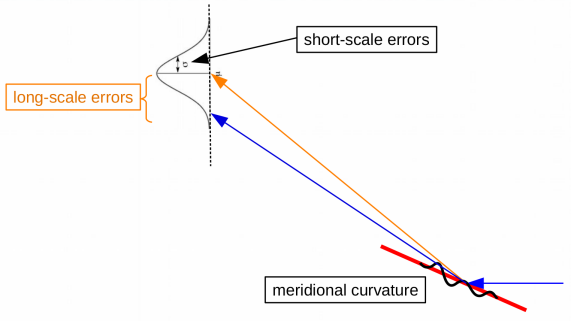

Figure 2.12: Depiction of the measurement process and three performance indicators derived from it. The X-ray beam enters from the right and impinges on a plate (in red) whose surface has some defects (represented by the black wavy line). These defects lead to a broadening of the reflected beam (short length-scale errors). The meridional curvature of the plate is also derived (global figure errors). Long-scale figure errors are arrived at by comparing the expected (blue arrow) and the measured (orange arrow) barycenter of the reflected beam, taking into account the best-fit meridional curvature.

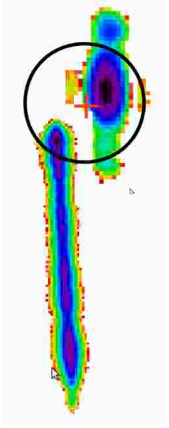

Figure 2.13: Illustration of the algorithm that leads to the construction of the on model centroid image for a stack. Shown are two of the reflected beam images. The cross at the center indicates the place where the barycenters of the reflected beams are expected to fall if the sample behaved ideally. A synthetic image, called the on model centroid image, is obtained by adding each reflected beam to it after applying the translation calculated during the analysis.

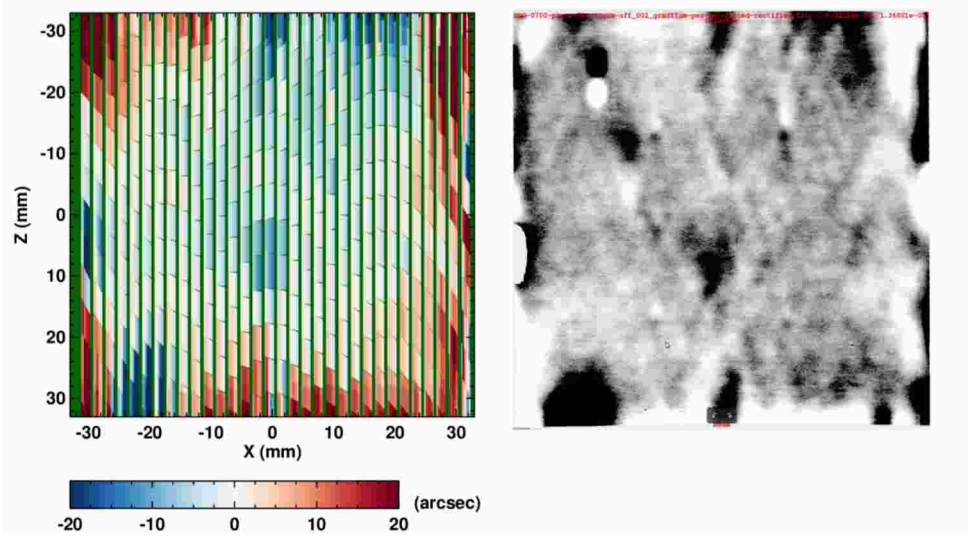

Figure 2.14: An example of a synoptic slope error map derived from X-ray data (left), compared to the cleanroom surface metrology for one of the plates in the same stack. The two independent datasets are in excellent agreement. Reproduced from [23].

for the entire stack: each block is made of a number of smaller rectangles, one for each plate, color coding the local slope error experienced by the X-ray beam (left to right for increasing plate number). These maps can be compared to similar per-plate maps obtained during manufacturing of the stack. It can be seen in the figure that the same features are visible in both maps. This proves that cleanroom metrology provides information that is immediately relevant for the X-ray behavior of the optics. The map also shows that the error experienced by the X-ray beam at each location is nearly the same irrespective of plate number. This shows that the shape of the first plate in the stack is almost exactly reproduced across the entire stack.

2.9.2 X-ray optical unit and mirror module characterization

Once assembled into an imaging system (XOU), a primary-secondary stack doublet can be characterized with the same standard scan used for the characterization of single stacks. The analysis of the data proceeds along the same lines described in the previous section, but now the individual images can be combined to arrive at an estimate of the HEW of the imaging system (Figure 2.15). Owing to the use of a pencil beam, it is now possible to analyze the performance of the optics along different axes, for instance by looking at how the HEW changes with plate number. Other spatial selections are possible, leading to the ability to compare the performance of different regions of the optics, that can be related to the indicators derived from the cleanroom metrology.

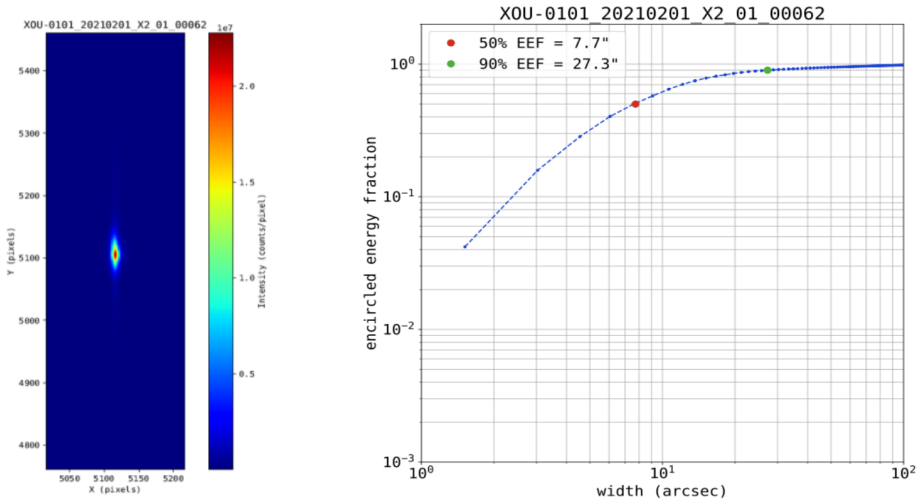

Figure 2.15: A sample PSF obtained by the algorithmic superposition of several thousands individual pencil-beam images. This particular image refers to the primary-secondary pair called XOU-0101, and it shows the result obtained for the central 70 % of the width of the sample. This has been a common data selection used during the development of SPO.

2.10 Conclusions and outlook

SPO uses technology spin-in developed for decades by the semiconductor and automotive industry, which have massively invested in the fabrication and processing of silicon wafers. It has become a very mature x-ray optics technology, thanks to the continuous development efforts to prepare the industrial production of Athena, the largest x-ray optics yet to be launched into space. SPO is an enabling technology for Athena, which could not aim for the combination of such a large effective area and high angular resolution with any other existing technology. The optics for Athena is under intense development, aiming to start manufacturing the first flight models MMs in 2026. SPO has also shown to be a versatile technology that can be further developed for gamma-ray optics and medical applications[24].

References

[1] M. Beijersbergen, S. Kraft, R. Günther, *et al.*, *Silicon pore optics: novel lightweight high-resolution X-ray optics developed for XEUS,* in *UV and Gamma-Ray Space Telescope Systems*, Vol. 5488, edited by G. Hasinger and M. J. L. Turner, International Society for Optics and Photonics (SPIE, 2004) pp. 868 – 874.

[2] M. Bavdaz, E. Wille, M. Ayre, *et al.*, *Optics developments for ATHENA,* in *Optics for EUV, X-Ray, and Gamma-Ray Astronomy IX*, Vol. 11119, edited by S. L. O'Dell and G. Pareschi, International Society for Optics and Photonics (SPIE, 2019) pp. 71 – 82.

[3] M. J. Collon, G. Vacanti, N. M. Barrière, *et al.*, *Status of the silicon pore optics technology,* in *Optics for EUV, X-Ray, and Gamma-Ray Astronomy IX*, Vol. 11119, edited by S. L. O'Dell and G. Pareschi, International Society for Optics and Photonics (SPIE, 2019) pp. 150 – 157.

[4] M. Shimbo, K. Furukawa, K. Fukuda, and K. Tanzawa, *Silicon-to-silicon direct bonding method,* Journal of Applied Physics **60**, 2987 (1986).

[5] W. P. Maszara, G. Goetz, A. Caviglia, and J. B. McKitterick, *Bonding of silicon wafers for silicon-on-insulator,* Journal of Applied Physics **64**, 4943 (1988).

[6] A. Jafari, D. D. M. Ferreira, S. Kadkhodazadeh, *et al.*, *Long-term performance and durability of Ir/B4C multilayer x-ray mirrors: focusing on composition, structure, and reflectivity properties,* Journal of Astronomical Telescopes, Instruments, and Systems **6**, 1 (2020).

[7] D. D. M. Ferreira, S. Svendsen, S. Massahi, *et al.*, *Performance and stability of mirror coatings for the ATHENA mission,* in *Space Telescopes and Instrumentation 2018: Ultraviolet to Gamma Ray*, Vol. 10699, edited by J.-W. A. den Herder, S. Nikzad, and K. Nakazawa, International Society for Optics and Photonics (SPIE, 2018) pp. 916 – 926.

[8] P. Gorenstein, *Focusing x-ray optics for astronomy,* X-Ray Optics and Instrumentation **2010** (2010), 10.1155/2010/109740.

[9] F. E. Christensen, A. C. Jakobsen, N. F. Brejnholt, *et al.*, *Coatings for the NuSTAR mission,* in *Optics for EUV, X-Ray, and Gamma-Ray Astronomy V*, Vol. 8147, edited by S. L. O'Dell and G. Pareschi, International Society for Optics and Photonics (SPIE, 2011) pp. 298 – 316.

[10] S. Massahi, F. E. Christensen, D. D. M. Ferreira, *et al.*, *Installation and commissioning of the silicon pore optics coating facility for the ATHENA mission,* in *Optics for EUV, X-Ray, and Gamma-Ray Astronomy IX*, Vol. 11119, edited by S. L. O'Dell and G. Pareschi, International Society for Optics and Photonics (SPIE, 2019) pp. 115 – 130.

[11] D. Girou, S. Massahi, D. D. M. Ferreira, *et al.*, *Plasma etching for the compatibility of thin film metallic coatings and direct bonding of silicon pore optics,* Journal of Applied Physics **128**, 095302 (2020), https://doi.org/10.1063/5.0010212 .

[12] W. KERN, *Cleaning solutions based on hydrogen peroxide for use in silicon semiconductor technology,* RCA Review **31**, 187 (1970).

[13] U. Gösele and Q.-Y. Tong, *Semiconductor wafer bonding,* Annual Review of Materials Science **28**, 215 (1998), https://doi.org/10.1146/annurev.matsci.28.1.215 .

[14] N. M. Barrière, G. Vacanti, S. Verhoeckx, *et al.*, *Assembly of confocal silicon pore optic mirror modules for Athena,* in *Optics for EUV, X-Ray, and Gamma-Ray Astronomy IX*, Society of Photo-Optical Instrumentation Engineers (SPIE) Conference Series, Vol. 11119 (2019) p. 111190J.

[15] N. M. Barrière, L. Babić, A. Bayerle, *et al.*, *Assembly of confocal silicon pore optics mirror modules,* in *Society of Photo-Optical Instrumentation Engineers (SPIE) Conference Series*, Society of Photo-Optical Instrumentation Engineers (SPIE) Conference Series, Vol. 11822 (2021) p. 1182208.

[16] E. Handick, L. Cibik, M. Krumrey, *et al.*, *Upgrade of the x-ray parallel beam facility XPBF 2.0 for characterization of silicon pore optics,* in *Society of Photo-Optical Instrumentation Engineers (SPIE) Conference Series*, Society of Photo-Optical Instrumentation Engineers (SPIE) Conference Series, Vol. 11444 (2020) p. 114444G.

[17] D. Heinis, A. Carballedo, C. Colldelram, *et al.*, *X-ray facility for the characterization of the Athena mirror modules at the ALBA synchrotron,* in *Society of Photo-Optical Instrumentation Engineers (SPIE) Conference Series*, Society of Photo-Optical Instrumentation Engineers (SPIE) Conference Series, Vol. 11852 (2021) p. 1185222.

[18] D. A. Girou, C. van Baren, I. te Kloeze, *et al.*, *Environmental testing of the Athena telescope mirror modules,* in *Optics for EUV, X-Ray, and Gamma-Ray Astronomy X*, Vol. 11822, edited by S. L. O'Dell, J. A. Gaskin, and G. Pareschi, International Society for Optics and Photonics (SPIE, 2021) pp. 47 – 55.

[19] M. J. Collon, S. Kraft, R. Günther, *et al.*, *Performance characterization of silicon pore optics,* (Orlando, Florida , USA, 2006) p. 62661T.

[20] M. Krumrey, L. Cibik, P. Müller, *et al.*, *X-ray pencil beam facility for optics characterization,* (San Diego, California, USA, 2010) p. 77324O.

[21] M. D. Ackermann, M. J. Collon, R. Guenther, *et al.*, *Performance prediction and measurement of silicon pore optics,* (San Diego, CA, 2009) p. 74371N.

[22] M. Krumrey, P. Müller, L. Cibik, *et al.*, *New x-ray parallel beam facility XPBF 2.0 for the characterization of silicon pore optics,* (Edinburgh, United Kingdom, 2016) p. 99055N.

[23] G. Vacanti, N. Barrière, M. Bavdaz, *et al.*, *Measuring silicon pore optics,* in *Optics for EUV, X-Ray, and Gamma-Ray Astronomy VIII*, Vol. 10399, edited by S. L. O'Dell and G. Pareschi, International Society for Optics and Photonics (SPIE, 2017) pp. 131 – 136.

[24] D. Girou, E. Ford, C. Wade, *et al.*, *Design and modeling of a laue lens for radiation therapy with hard x-ray photons,* Physics in Medicine & Biology **66**, 245007 (2021).